Anderson localization induced by spin-flip disorder in large-Chern-number quantum anomalous Hall effect

Hui Yang,[1] Junjie Zeng,[1] Yulei Han,[1,2,*] and Zhenhua Qiao[1,†]

[1]*ICQD, Hefei National Laboratory for Physical Sciences at Microscale, CAS Key Laboratory of Strongly-Coupled Quantum Matter Physics, and Department of Physics, University of Science and Technology of China, Hefei, Anhui 230026, China*

[2]*Department of Physics, Fuzhou University, Fuzhou, Fujian 350108, China*

(Received 27 March 2020; revised 25 August 2021; accepted 25 August 2021; published 13 September 2021)

We numerically investigate the localization mechanisms of the quantum anomalous Hall effect (QAHE) with a large Chern number $\mathcal{C}$ in bilayer graphene and magnetic topological insulator thin films doped with nonmagnetic or spin-flip (magnetic) disorder. By calculating the modified Berry curvature in real space, we demonstrate that QAHEs in both systems turn into Anderson insulators when the disorder strength is large enough in the presence of nonmagnetic disorder. However, in the presence of spin-flip disorder, the localization mechanisms in the two systems are completely distinct. For ferromagnetic bilayer graphene with Rashba spin-orbit coupling, the QAHE with $\mathcal{C} = 4$ first enters a metallic phase and then turns into an Anderson insulator with the increase of disorder strength, whereas for magnetic topological insulator thin films, the QAHE with $\mathcal{C} = -\mathcal{N}$ first enters a metallic phase, then turns into another QAHE with $\mathcal{C} = -(\mathcal{N} - 1)$ as disorder strength increases, and finally turns into an Anderson insulator after $\mathcal{N} - 1$ cycles between QAHE and metallic phases. The phase transitions in the two systems originate from the exchange of Berry curvature between conduction and valence bands. In the end, we provide a phenomenological picture related to the topological charges to help understand the underlying physical origins of the two different phase-transition mechanisms.

DOI: 10.1103/PhysRevB.104.115414

I. INTRODUCTION

Anderson localization is one of the most striking transport phenomena in condensed matter physics [1]. It describes the absence of diffusion of waves in a disordered medium. It is well known that two-dimensional electrons can be suddenly driven into the Anderson insulating phase even in the presence of extremely weak disorders. When the time-reversal symmetry is broken by applying magnetic fields, or the spin-rotational symmetry is broken by the presence of spin-orbit coupling, a metal-insulator phase transition appears, indicating that a metallic phase emerges at weak disorders [2–4].

Ever since the experimental realization of graphene [5–7] and topological insulators [8,9], much attention has been paid to exploring the long-sought quantum anomalous Hall effect (QAHE) [10–37], which was first experimentally observed in magnetic topological insulator thin films [38]. In the conventional quantum Hall effect (QHE) induced by strong magnetic field [39,40], several different localization mechanisms have been proposed, such as levitation theory, pointing out that the phase transition can only occur in the nearest-neighbor Hall plateaus, and a global phase diagram has been established [41]. Meanwhile, Sheng *et al.* [42] propose that quantum Hall plateaus are destroyed in a one-by-one order from high to low energies without floating up in energy. Compared with QHE, the QAHE demonstrates similar bulk-edge relation and edge state transport properties. However, the QAHE requires a nontrivial exchange gap at the Dirac point, which is different from the formation of discrete Landau levels in QHE [43,44]. And the spin/pseudospin degree of freedom plays a crucial role in the formation of QAHE. The previous works demonstrate that QAHE with a Chern number of $\mathcal{C} = 1$ turns into an Anderson insulator in two different ways, depending on the types of disorders, i.e., (i) QAHE→Anderson insulator in the presence of nonmagnetic disorder, and (ii) QAHE→metal→Anderson insulator in the presence of spin-flip disorder [45,46]. However, the localization mechanism of QAHE with a large Chern number (multiple edge states) is still lacking, and disorders often do not act on the spin space of the system [47–51].

In this work, we investigate the electronic transport properties of the chiral edge modes in large-Chern-number QAHE systems, i.e., bilayer graphene and magnetic topological insulator thin films, in the presence of nonmagnetic and spin-flip disorders. In a ferromagnetic bilayer graphene system with Rashba spin-orbit coupling, the QAHE with a Chern number of $\mathcal{C} = 4$ can be formed. In magnetic topological insulator thin films, the QAHE with different Chern numbers can be produced by tuning the ferromagnetism strength (film thickness) at fixed film thickness (ferromagnetism strength). In the presence of nonmagnetic disorder, both systems enter Anderson insulators from the QAHE phase without entering another QAHE phase; whereas in the presence of spin-flip disorder, we find that (i) in the bilayer graphene system, the QAHE with a Chern number of $\mathcal{C} = 4$ first enters a metallic phase, then turns into an Anderson insulator with increasing disorder strength; (ii) in the magnetic topological insulator thin film

*hanyulei@ustc.edu.cn
†qiao@ustc.edu.cn

 ©2021 American Physical Society

system, the QAHE with a Chern number of $\mathcal{C} = -\mathcal{N}$ first enters a metallic phase, then enters another QAHE phase with $\mathcal{C} = -(\mathcal{N}-1)$, and finally turns into a localized Anderson insulator phase after $\mathcal{N}-1$ cycles between the QAHE and metallic phases. In the end, we provide a phenomenological picture of spin-texture evolutions to understand the underlying physical mechanisms of Anderson localization phenomena induced by two different disorders.

II. SYSTEM MODELS AND METHODS

In our research, we select the AB-stacked bilayer graphene and magnetic topological insulator thin films to realize the large-Chern-number QAHE, respectively. The tight-binding Hamiltonian of the ferromagnetic bilayer graphene in the presence of Rashba spin-orbit coupling can be expressed as [28,52]

$$H_{\mathrm{BLG}} = H_{\mathrm{SLG}}^{\mathrm{T}} + H_{\mathrm{SLG}}^{\mathrm{B}} + t_{\perp} \sum_{i\in \mathrm{T}, j\in \mathrm{B},\alpha} c_{i\alpha}^{\dagger} c_{j\alpha}, \tag{1}$$

$$H_{\mathrm{SLG}} = -t \sum_{\langle ij\rangle\alpha} c_{i\alpha}^{\dagger} c_{j\alpha} + i t_{\mathrm{R}} \sum_{\langle ij\rangle\alpha\beta} (\boldsymbol{s}_{\alpha\beta} \times \mathbf{d}_{ij}) \cdot \hat{\mathbf{z}} c_{i\alpha}^{\dagger} c_{j\beta} + M \sum_{i\alpha} c_{i\alpha}^{\dagger} (s_z)_{\alpha\alpha} c_{i\alpha}, \tag{2}$$

where $H_{\mathrm{SLG}}^{\mathrm{T,B}}$ represents the Hamiltonian of the top (T) or bottom (B) graphene layer. $t_{\perp}$ is the interlayer hopping amplitude. In Eq. (2), the first term describes the nearest-neighbor hopping; the second term represents the Rashba spin-orbit coupling with a coupling strength of t_{R}, and $\mathbf{d}_{ij}$ is the unit vector pointing from j-site to i-site; the third term refers to the exchange field with a field strength of M. Here, α and β denote spin indices.

The tight-binding Hamiltonian of the magnetic topological insulator thin films can be written as [53]

$$H = \sum_i \varepsilon_0 c_i^{\dagger} c_i + \sum_i \sum_{\gamma=x,y,z} c_i^{\dagger} T_{\gamma} c_{i+\gamma} + \mathrm{H.c.} + \sum_i m_0 c_i^{\dagger} c_i, \tag{3}$$

where $\varepsilon_0 = (C - 3B/2)\tau_z \otimes \sigma_0$, $T_{\gamma} = B/4\tau_z \otimes \sigma_0 - iA/2\tau_x \otimes \sigma_{\gamma}$, and $m_0 = m\tau_0 \otimes \sigma_z$. $c_i = [a_{i\uparrow}, a_{i\downarrow}, b_{i\uparrow}, b_{i\downarrow}]$, with (a, b) denoting two independent orbitals and $(\uparrow\downarrow)$ representing spin indexes. A, B, and C are independent parameters, with A referring to the Fermi velocity and C determining the amplitude of the inverted band gap. γ refers to the unit vector towards the direction of $\gamma = (x, y, z)$. σ and τ are, respectively, spin and orbital Pauli matrices. m measures the effective exchange field strength. Since we focus on the resulting topological phenomena of magnetic topological insulator thin films, the thickness (i.e., layer number) along the z-direction is set to be finite [32].

In both cases, we apply either nonmagnetic or spin-flip disorder to investigate the transport properties of the large-Chern-number QAHE. The tight-binding Hamiltonian of the applied disorders can be expressed as

$$H_{\mathrm{dis}} = \sum_i w_i^0 c_i^{\dagger} c_i + w_i^x c_i^{\dagger} \sigma_x c_i + w_i^y c_i^{\dagger} \sigma_y c_i, \tag{4}$$

where the first term describes the on-site nonmagnetic disorder, and the last two terms correspond to spin-flip disorder. $w_{0,x,y}$ are uniformly distributed in the interval of $[-W/2, W/2]$, with W representing the disorder strength. In our study, we use the Landauer-Büttiker formula to calculate the two-terminal conductance of the large-Chern-number QAHE in the presence of either nonmagnetic or spin-flip disorder. The disorders are only considered in the central scattering region that couples with two semi-infinite leads, which are exactly extended from the central part. The conductance from the left to right terminal can be evaluated as [54]

$$G_{\mathrm{LR}} = \frac{2e^2}{h} \mathrm{Tr}[\Gamma_{\mathrm{L}} G^{\mathrm{r}} \Gamma_{\mathrm{R}} G^{\mathrm{a}}], \tag{5}$$

where $G^{\mathrm{r,a}}$ are, respectively, the retarded and advanced Green's functions, and $\Gamma_{\mathrm{L,R}}$ are the linewidth functions coupling with the left and right terminals.

III. RESULTS AND DISCUSSIONS

In bilayer graphene, the formation of QAHE requires typically the application of Rashba SOC and an exchange field, whereas in a magnetic topological insulator, the realization of QAHE only requires the exchange field. Figures 1(a)–1(d) show the band structures of the bilayer graphene with different Rashba SOC and exchange field strengths. In Fig. 1(a), one can see the band structure of the pristine bilayer graphene with double degeneracy and quadratic dispersion relations at K and K'. When Rashba SOC is exclusively applied, spin degeneracy is lifted and a linear dispersion relation appears [see Fig. 1(b)]. When the exchange field is exclusively turned on, the spin-up (spin-down) bands are pushed upwards (downwards), as shown in Fig. 1(c). When both Rashba SOC and the exchange field are considered, a topologically nontrivial band gap with a Chern number of $\mathcal{C} = 4$ appears around K/K'. Unlike bilayer graphene, the Dirac points emerge one by one as a function of exchange field in the magnetic topological insulator. The first Dirac point appears at $m = 2.465B$ [see Fig. 1(e)]. When the exchange field strength decreases to $m = 2.2B$, a topologically nontrivial band gap with a Chern number of $\mathcal{C} = -1$ exists [see Fig. 1(f)]. At $m = 1.963B$, the second Dirac point appears [see Fig. 1(g)]. And at $m = 1.75B$, the system is a QAHE insulator with a Chern number of $\mathcal{C} = -2$ [see Fig. 1(h)]. The localization mechanism of QAHE ($\mathcal{C} = 1$) in the presence of spin-flip disorder has been investigated. When spin-flip disorder strength exceeds a critical value, the quantized conductance at the charge neutrality point abruptly vanishes due to the interchange of Berry curvatures carried by the conduction and valence bands. For the nonmagnetic disorder case, the QAHE develops into an Anderson insulator directly without the interchange of Berry curvatures [45]. Two factors are crucial in localization phenomena of high Chern number systems, i.e., the types of bulk bands and the mechanisms of Hall conductivity destroyed by disorders. In the following, we will describe these phenomena in detail.

A. Localization mechanism for bilayer graphene-based QAHE

In a bilayer graphene-based QAHE system, we select several representative Fermi energies inside the bulk band

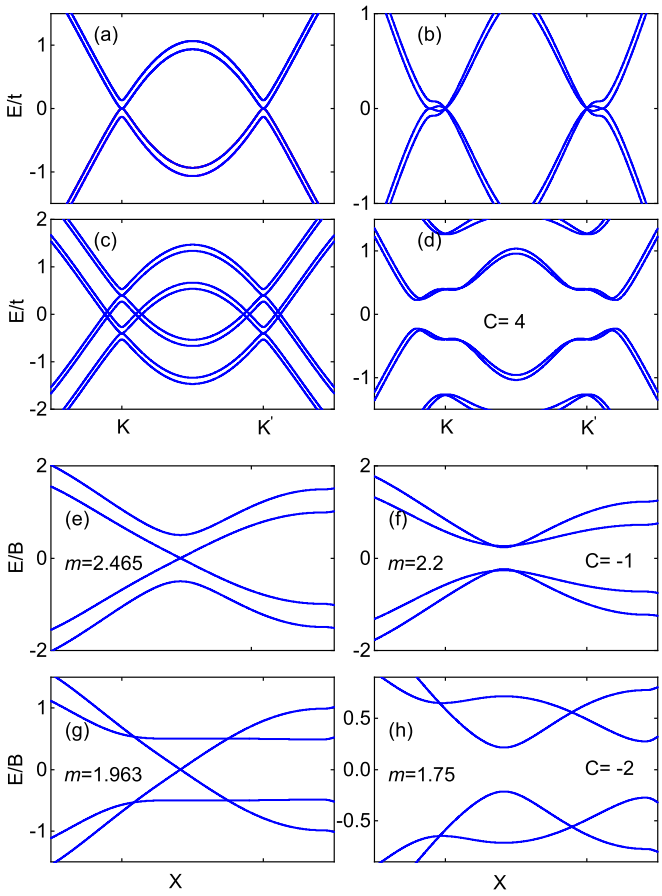

FIG. 1. The bulk band structures for bilayer graphene. (a) Pristine bilayer graphene. (b) When only $t_R = 0.4t$ is applied. (c) When only exchange field $M = 0.4t$ is applied, the spin-up/spin-down bands are upwards/downwards lifted with the bands crossing near K and K' points. (d) When Rashba SOC $t_R = 0.4t$ and exchange field $M = 0.4t$ both exist, a bulk gap is opened and the system is a QAHE insulator with $\mathcal{C} = 4$. (e)–(h) The bulk band spectra along the high-symmetry lines of the magnetic element doped topological insulator films in the presence of different exchange field strength (e) $m = 2.465B$, (f) $m = 2.2B$, $\mathcal{C} = -1$, (g) $m = 1.963B$, and (h) $m = 1.75B$, $\mathcal{C} = -2$. The corresponding system parameters are set as $C = 0.3B$, $A = 0.5B$, $N_z = 2$ (layer number).

gap, such as $E_F/t = 0.001$, 0.04, 0.08, 0.12, 0.16, and 0.20, to investigate how disorders affect the electronic transport properties. Figure 2 depicts the averaged two-terminal conductance $\langle G\rangle$ as a function of the disorder strength W for nonmagnetic and spin-flip disorders. For the nonmagnetic case as displayed in Fig. 2(a), the conductance remains quantized with $\langle G\rangle = 4e^2/h$ in the presence of weak disorders. Around the critical value of disorder strength, the conductance shows a rapid decrease. As disorder strength increases, the conductance shows a gradual decrease to zero. Particularly at a fixed disorder strength, the closer the Fermi energy is to the charge neutrality point $E_F/t = 0.00$, the more it takes for the quantized conductance to be destroyed. In contrast, for the spin-flip disorder, the effects of disorder on the electronic transport properties are completely different from those observed in the former case. Figure 2(b) shows the averaged conductance as a function of disorder strength in the presence of spin-flip disorder. One can find that the variation of the averaged conductance is divided into two parts with the increase of disorder strength, i.e., (i) in the presence of weak disorders, the averaged conductance remains quantized with $\langle G\rangle = 4\,e^2/h$ before it reaches the critical disorder strength; (ii) once disorder strength exceeds the critical value, the averaged conductance gradually decreases and finally vanishes. Contrary to the nonmagnetic case, the farther the Fermi energy is away from the charge neutrality point $E_F/t = 0.00$, the more it takes for the conductance to vanish. For instance, the averaged conductance for $E_F/t = 0.001$ remains quantized until ($W/t \approx 2.2$), and once $W/t > 2.3$, it immediately drops to zero.

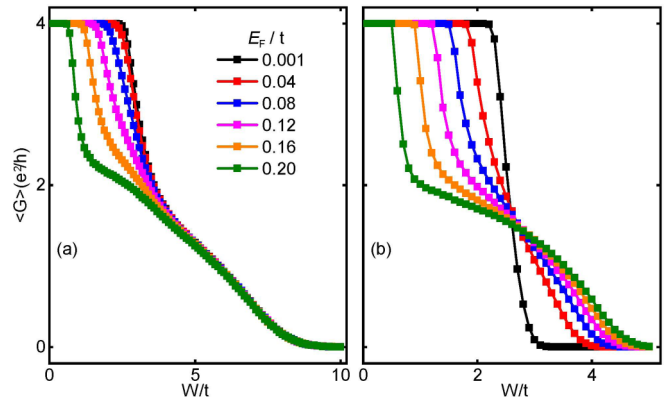

FIG. 2. Averaged conductance $\langle G\rangle$ as a function of W for different Fermi energies inside the bulk gap. The system is bilayer graphene with parameters set to be $N = 60$, $t_R = 0.4t$, and $M = 0.4t$. (a) and (b) For nonmagnetic and spin-flip disorders, respectively. 4000 samples are collected for each data point.

B. Localization mechanism for magnetic topological insulator thin film based QAHE

In magnetic topological insulator thin films, Fig. 3 displays the averaged conductance as a function of disorder strength for different Fermi energies inside the bulk gap. In the presence of nonmagnetic disorder [see Fig. 3(a)], the variation of averaged conductance with the increase of disorder strength is similar to the nonmagnetic case in a bilayer graphene system [see Fig. 2(a)]. But in the presence of spin-flip disorder, as shown in Fig. 3(b), the system exhibits a completely different localization phenomenon in contrast to that in bilayer graphene. The most striking feature is the appearance of an additional quantized conductance plateau with the increase of disorder strength W, i.e., in the presence of weak disorders, the averaged conductance remains quantized with a value of $\langle G\rangle = 2e^2/h$; when W reaches the first critical value (e.g., $W_{C1}/B \approx 1.90$ at $E_F/B = 0.001$), the initial quantized plateau is destroyed and the system quickly enters a lower quantized plateau with a value of $\langle G\rangle = e^2/h$; as W continues to increase, the averaged conductance remains quantized at $\langle G\rangle = e^2/h$; when W reaches the second critical point (e.g., $W_{C2}/B \approx 3.90$ at $E_F/B = 0.001$), the quantized plateau is destroyed and the conductance gradually vanishes. We can find that the closer the Fermi energy is to $E_F/B = 0.00$, the more it takes for the lower quantized conductance to be destroyed. As

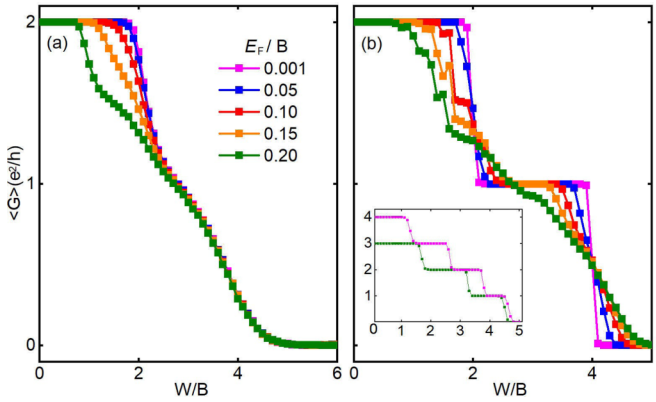

FIG. 3. Averaged conductance $\langle G\rangle$ as a function of W for different Fermi energies inside the bulk gap. The system is magnetic topological insulator thin films with width set to be $N = 80$. (a) and (b) For nonmagnetic and spin-flip disorders, respectively. 4000 samples are collected for each data point. The inset of (b) is the conductance variation of the system with a higher Chern number in $E_F/B = 0.002$. 150 samples are collected for each data point. The parameters in the inset are $C = 0.3B$, $A = 0.5B$, $m = 1.71B$, $N = 60$ for $\mathcal{C} = -4$, and $C = 0.3B$, $A = 0.5B$, $m = 1.7B$, $N = 60$ for $\mathcal{C} = -3$, respectively.

a consequence, the lower quantized plateau almost disappears at the conduction-band edge ($E_F/B = 0.20$).

For magnetic topological insulator thin films, the Chern number can be tuned by varying the thickness of the films. The inset of Fig. 3(b) shows the averaged conductance as a function of disorder strength for the system of $\mathcal{C} = -4$ and -3 at $E_F/B = 0.002$. One can see that the Hall conductance is destroyed step by step in a quantized manner. To understand the fundamental physics that results in these anomalous transport properties, we analyze the Berry curvature density in the corresponding bulk system that reflects the nature of QAHE.

C. Berry curvature analysis

For the disordered system, we use a Berry curvature and Kubo formula in real space to calculate Hall conductance, which can be stated, respectively, as [55]

$$\Omega_\alpha = -\sum_{\beta\neq\alpha} \frac{2\,\mathrm{Im}\langle\alpha|v_x|\beta\rangle\langle\beta|v_y|\alpha\rangle}{(w_\alpha - w_\beta)^2}, \tag{6}$$

$$\sigma_{xy} = -\frac{e^2}{h}\int \langle\Omega(\epsilon)\rangle f(\epsilon)d\epsilon. \tag{7}$$

In the above equations, $\Omega(\epsilon) = \frac{1}{S}\mathrm{Tr}[\hat{\Omega}\delta(\epsilon - H)]$ describes the Berry curvature density in the energy spectrum with the Berry curvature operator $\hat{\Omega} = \sum_\alpha \Omega_\alpha|\alpha\rangle\langle\alpha|$, and $|\alpha\rangle$ indicates the eigenvector of $|\hbar w_\alpha\rangle$ in the disordered system. S is the area of the two-dimensional system, $v_{x/y}$ is the velocity operator in the x or y direction, and $f(\epsilon)$ is the Fermi-Dirac distribution.

The transport properties of bilayer graphene in the presence of nonmagnetic/spin-flip disorder are almost the same as those in the Qi-Wu-Zhang model with Chern number $\mathcal{C} = 1$ and monolayer graphene with Chern number $\mathcal{C} = 2$, which have been studied in our previous paper [45]. Therefore, in this article, we mainly explore the mechanisms of anomalous transport properties in magnetic topological insulator thin films. Figure 4 shows the averaged Berry curvature density Ω and Hall conductance σ_{xy} as a function of the Fermi

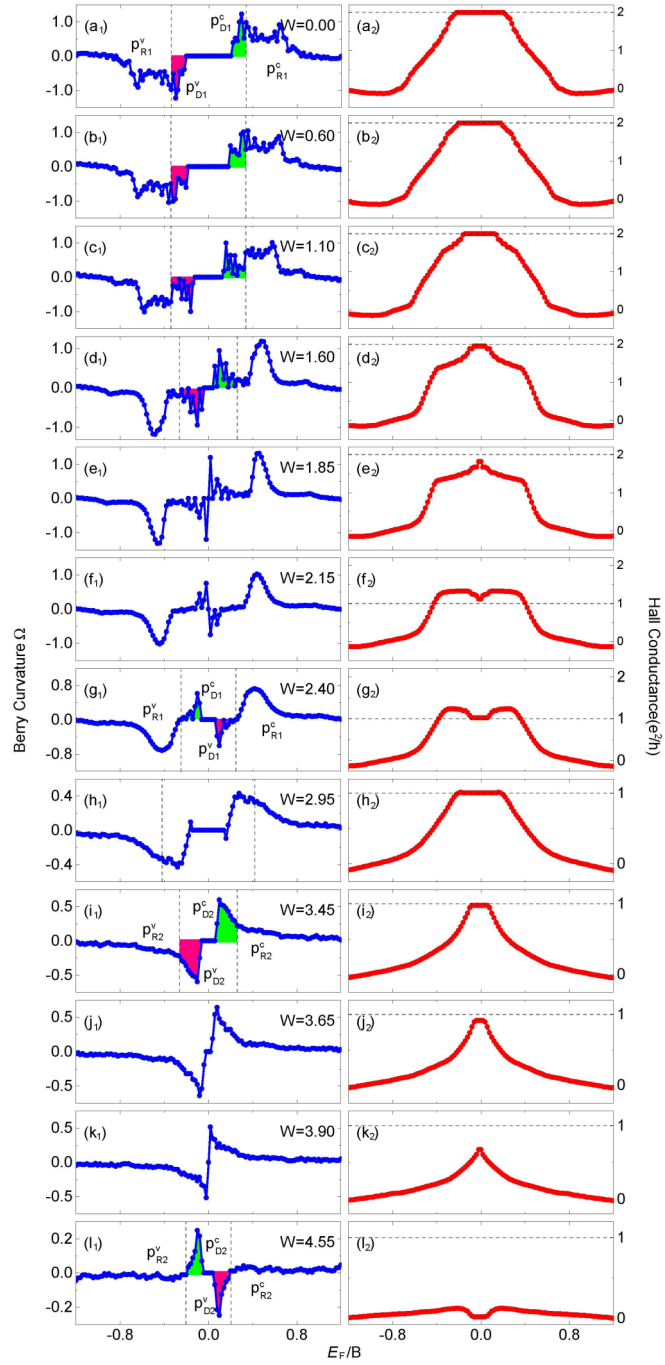

FIG. 4. (a_1)–(l_1) Averaged Berry curvature density Ω as a function of energy E for different spin-flip disorder strengths W in magnetic topological insulator thin films. (a_2)–(l_2) Corresponding averaged Hall conductance σ_{xy} as a function of energy E. $P^{v,c}_{D1}$ ($P^{v,c}_{D2}$) represent the Berry curvature contributed by the massive Dirac bands in the first (second) exchange process. $P^{v,c}_{R1}$ ($P^{v,c}_{R2}$) represent the Berry curvature contributed by the remaining bands in the first (second) exchange process. v (c) denotes valence (conduction) bands. 30 samples are collected for each point.

energy E for different spin-flip disorder strengths $W/B =$ 0.00, 0.60, 1.10, 1.60, 1.85, 2.15, 2.40, 2.95, 3.45,3.65,3.90, 4.25, and 4.55, respectively. At $W/B = 0.00$ [see Fig. 4(a_1)], we can identify two Berry curvature peaks in valence bands and conduction bands as $P_{D1}^{v,c}$, which originate from the contribution of massive Dirac bands, while $P_{R1}^{v,c}$ denotes the contribution of remaining bands, in which v/c denotes valence/conduction bands and $D1/R1$ denotes the massive Dirac/remaining bands for the first exchange process. One can find that for Fermi energies inside the bulk band gap, $\Omega(E) = 0$ and $\sigma_{xy} = 2e^2/h$, and the Hall conductance preserves $\sigma_{xy}(E) = \sigma_{xy}(-E)$, due to the electron-hole symmetry of energy bands. In the presence of weak disorders [see Figs. 4(b)–4(d)], the two Berry curvature peaks $P_{D1}^{v,c}$ move towards each other and shrink the band gap. The contribution of areas covered by red/green to Hall conductance is about $\pm 0.5e^2/h$. Meanwhile, the two Berry curvature peaks $P_{R1}^{v,c}$ are almost fixed and broadened. When the disorder strength approaches the first critical point $W/B \approx 1.85$ [Fig. 4(e)], the bulk gap begins closing and the Berry curvature peaks $P_{D1}^{v,c}$ start to exchange with each other. As the disorder strength continues to increase [see Figs. 4(f)–4(h)], one can find that the two Berry curvature peaks $P_{D1}^{v,c}$ make an interchange with the bulk gap reopening, and the Hall conductance inside the bulk gap now becomes $\sigma_{xy} = e^2/h$, which is consistent with the above transport calculations. At even stronger disorders [see Fig. 4(i)], one can see that the two Berry curvature peaks $P_{R1}^{v,c}$ vanish, and two new peaks appear, which can be identified as $P_{D2}^{v,c}$ followed by the similar definitions above. When the disorder strength is stronger [see Figs. 4(j)–4(l)], the two peaks $P_{D2}^{v,c}$ complete the second interchange process, and finally the Hall conductance inside the bulk gap is zero, indicating an Anderson insulator phase exists.

Figure 5 displays how the averaged Berry curvature density and Hall conductance evolve in magnetic topological insulator thin films with nonmagnetic disorder for comparison. With the increase of disorder strength, although the two Berry curvature peaks move towards each other and the bulk gap shrinks, the most noticeable difference from the case of spin-flip disorder is the lack of interchange of Berry curvature carried by massive Dirac bands. Therefore, the system with nonmagnetic disorder does not undergo a Berry curvature interchange but turns directly from the QAHE state into the Anderson insulating phase.

D. A phenomenological picture

As stated in Ref. [56], the Hall conductance can be expressed as

$$\sigma_{xy} = -\frac{1}{4\pi}\iint_{\mathrm{FBZ}} dk_x dk_y \hat{\mathbf{d}} \cdot \partial_x \hat{\mathbf{d}} \times \partial_y \hat{\mathbf{d}}, \tag{8}$$

where $\hat{\mathbf{d}}$ describes the spin part of the Hamiltonian, and it is also the mapping from the Brillouin zone to the unit sphere. The $\hat{\mathbf{d}} \cdot \partial_x \hat{\mathbf{d}} \times \partial_y \hat{\mathbf{d}}$ is the Jacobian of this mapping. The quantized Hall conductance measures the skyrmion number in this model. In the ferromagnetic graphene system with Rashba spin-orbit coupling [29], two skyrmions located at two valleys give rise to a total Chern number of $\mathcal{C} = 2$. In the presence of disorders, the Hall conductance (Chern number) still counts

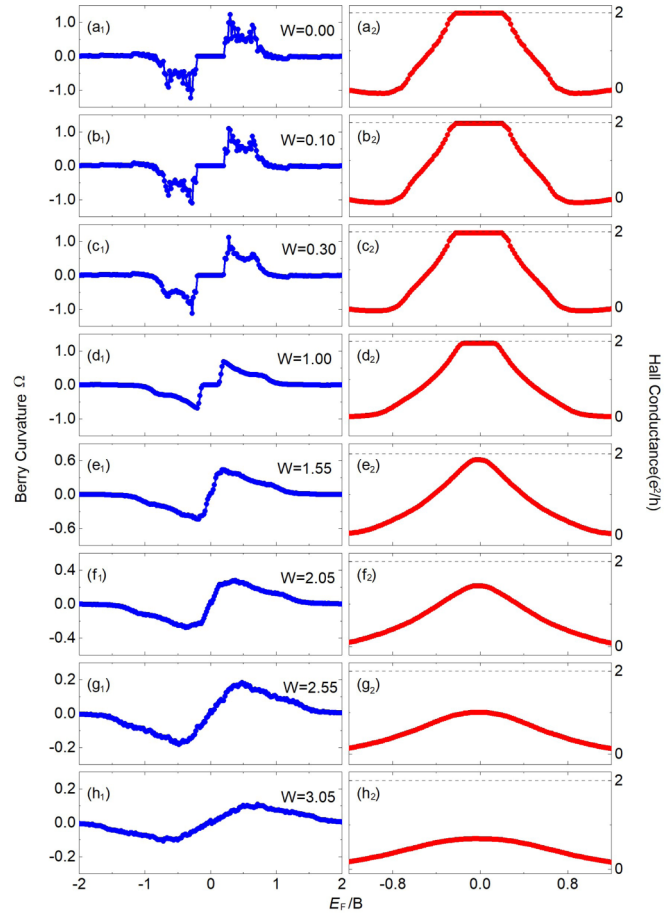

FIG. 5. (a_1)–(h_1) Averaged Berry curvature density Ω as a function of energy E for different nonmagnetic disorder strengths W in magnetic topological insulator thin films. (a_2)–(h_2) Corresponding averaged Hall conductance σ_{xy} as a function of energy E. 30 samples are collected for each point.

the number of topological charges and is quantized, as long as the ground state is nondegenerate and separated from the excited states by a finite energy gap [57–59]. We present an illustrative analogy by considering the Chern numbers as combinations of skyrmions.

The quantized Hall conductance of $\sigma_{xy} = -e^2/h$ is analogous to a skyrmion, where the valence or conduction bands carry a topological charge of $Q_{v/c} = \pm 1$ [45] depending on the spin textures [60]. In a skyrmion with a unit of positive (negative) topological charge, the spin points upwards (downwards) at the north pole, downwards (upwards) at the south pole, and in-plane at the equator, as vividly displayed in Fig. 6. In the absence of disorders, valence and conduction bands carry four topological charges labeled as "A," "B," "C," and "D" [see Fig. 6(a)]. When the spin-flip disorder is applied [see Fig. 6(b)], all skyrmions are divided into eight merons (labeled as "A1," "A2," "B1," "B2," "C1," "C2," "D1," and "D2"). As shown in Fig. 6(c), merons B2 and C1 move towards each other in an attractive manner when the disorder strength reaches the first critical point. As disorder strength increases, merons B2 and C1 move into the valence and conduction bands, respectively [see Fig. 6(d)]. Thus, the Hall conductance in valence bands transits into the lower plateau

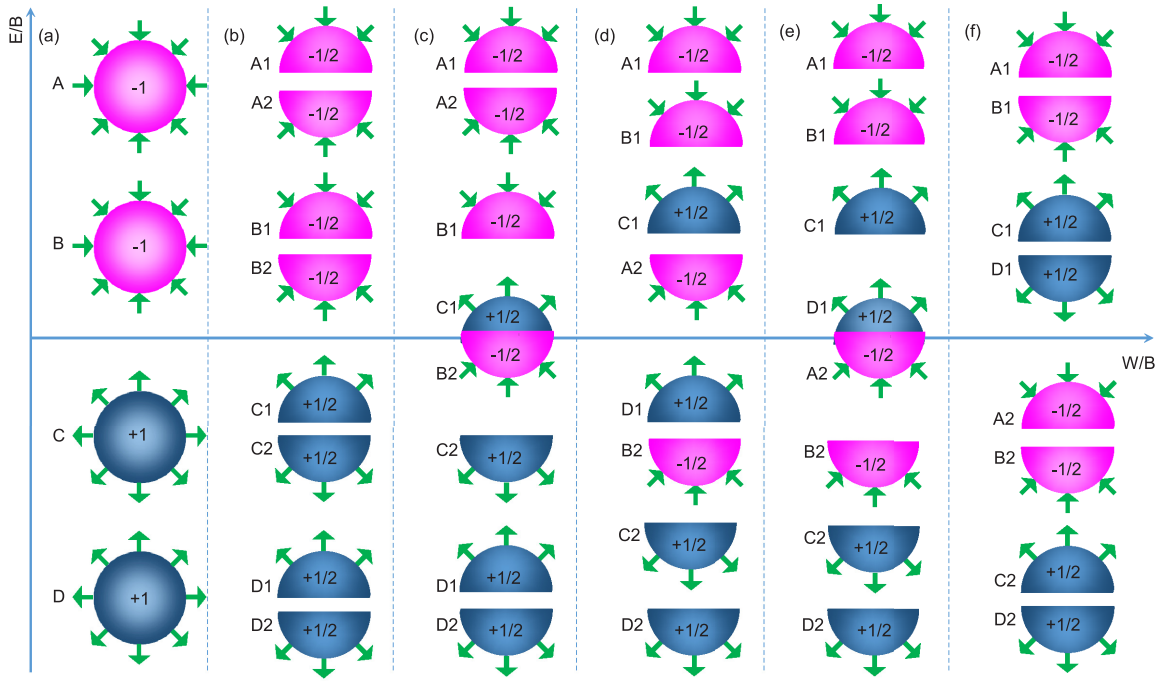

FIG. 6. Schematic of topological charges carried by the spin textures of the valence and conduction bands in magnetic topological insulator thin films with spin-flip disorder. (a) In the absence of disorders, valence/conduction bands carry four skyrmions with topological charges of $+1$, $+1$, -1, and -1. (b) At weak disorders, four skyrmions are scattered to eight merons that carry half-integer topological charges and are labeled as "A1,""A2," "B1," "B2," "C1," "C2," "D1," and "D2." (c) By further increasing disorder strength, merons B2 and C1 move towards each other. (d) Merons B2 and C1 make an exchange, leading to Hall conductance falling on the next ladder. (e) and (f) Weak disorders hardly affect merons A2 and D1. When the disorder strength approaches the second critical point, merons A2 and D1 move towards each other and make an exchange, which results in the disappearance of integer conductance.

$\sigma_{xy} = e^2/h$. It is noteworthy that merons D1 and A2 are not influenced by the spin-flip disorder until disorder strength approaches the second critical point. As disorder strength continuously increases [see Figs. 6(e)–6(f)], merons D1 and A2 first move towards each other, then partially overlap, and finally exchange with each other. Meanwhile, the Hall conductance disappears and the system enters the Anderson insulator phase. Figure 7 displays the evolution of topological charges carried by the spin-textures of the valence and conduction bands in a bilayer graphene system. In the presence of weak disorders [see Figs. 7(a)–7(b)], four skyrmions are divided into eight merons labeled as "A1," "A2," "B1," "B2,"

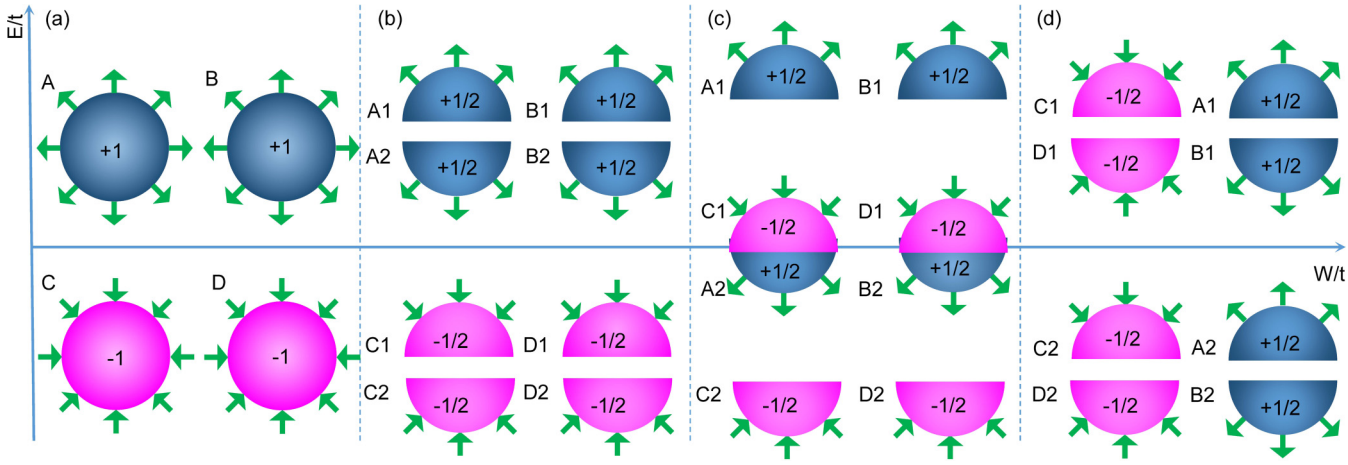

FIG. 7. Schematic of topological charges carried by the spin textures of the valence and conduction bands in bilayer graphene with spin-flip disorder. (a) In the absence of disorders, valence/conduction bands carry four skyrmions with topological charges of $+1$, $+1$, -1, and -1. (b) At weak disorders, four skyrmions are scattered to eight merons that carry half-integer topological charges and are labeled as "A1,""A2," "B1," "B2," "C1," "C2," "D1," and "D2." (c) By further increasing disorder strength, merons, A2 and C1, B2 and D1 move towards each other. (d) At strong disorders, merons A2,C1 and B2,D1 and make an exchange, causing the disappearance of quantized Hall conductance.

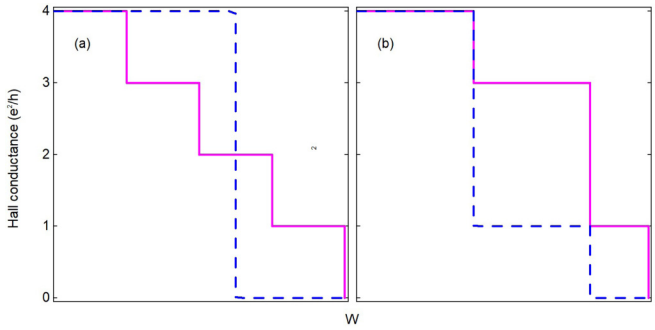

FIG. 8. Spin-flip disorder dependence of Hall conductance. (a),(b) Sketch of Hall conductance as a function of spin-flip disorder strength W, which can/cannot be realized in the magnetic topological insulator thin films and bilayer graphene.

"C1," "C2," "D1," and "D2." Each meron carries half-integer topological charge. When the disorder strength is stronger [see Fig. 7(c)], the merons A2,C1 and B2,D1 do not make an interchange step by step, but interchange simultaneously. After the interchange [see Fig. 7(d)], the net charge in valence bands is zero, indicating the system enters the Anderson insulating phase.

By analyzing the Berry curvature of magnetic topological insulator thin films, we find that none of topological charges are equivalent in magnetic topological insulator thin films, and the different responses of topological charges to spin-flip disorder lead to the sequential charge destruction. But in bilayer graphene, all the topological charges are equivalent, leading to simultaneous destruction of topological charges and direct jump of Hall conductance from maximum to zero in the presence of spin-flip disorder. Therefore, the decrease of Hall conductance as a function of spin-flip disorder strength follows $\mathcal{N} \to \mathcal{N} - 1$ or $\mathcal{N} \to 0$, as shown in Fig. 8(a). However, with the increase of spin-flip disorder strength, the Hall conductance cannot be destroyed through $4 \to 1 \to 0$ or $4 \to 3 \to 1 \to 0$ as displayed in Fig. 8(b).

IV. CONCLUSION

We numerically investigate disorders effects (including nonmagnetic disorder and spin-flip disorder) on two types of large-Chern-number QAHE systems. In the presence of nonmagnetic disorder, both systems display similar localization behavior that turns from the QAHE state into the Anderson insulating state without undergoing a Berry curvature interchange process. In the presence of spin-flip disorder, we find that the metallic phase exists in both systems with the increase of disorder strength, but the mechanisms of phase transition are different. In magnetic topological insulator thin films, the quantized conductances are destroyed step by step from higher to lower integer plateau, and finally the system enters the Anderson insulating phase; while in bilayer graphene, the quantized conductances are destroyed only in one step and eventually the system becomes the Anderson insulator. The underlying physical mechanisms in the two types of QAHE systems can be explained from the view of topological charges, which are, respectively, carried by valence/conduction bands. Our work provides a deep understanding of disorder effects on the QAHE systems with a tunable Chern number.

ACKNOWLEDGMENTS

This work was financially supported by the National Natural Science Foundation of China (Grant No. 11974327), Fundamental Research Funds for the Central Universities (WK3510000010, WK2030020032) and Anhui Initiative in Quantum Information Technologies. We are grateful to the supercomputing service of AM-HPC and the Supercomputing Center of USTC for providing the high-performance computing resources.

APPENDIX A: DERIVATION OF THE BERRY CURVATURE FORMULA IN THE NONPERIODIC SPACE

In this Appendix, we will illustrate how the Berry curvature transforms from a periodic space to a nonperiodic space. Equations (A1)–(A3) show the definition of Berry curvature in periodic systems, whereas Eqs. (A4)–(A8) show the definition of Berry curvature in nonperiodic systems.

In the noninteracting electronic system, the topological property of a two-dimensional band insulator is characterized by the quantized charge Hall conductance [40,61]:

$$\sigma_{xy} = \mathcal{C}\frac{e^2}{h}, \tag{A1}$$

where $\mathcal{C}$ is an integer known as the first Chern number, and it can be calculated by integrating the Berry curvature over the first Brillouin zone (BZ) [61,62]:

$$\mathcal{C} = \frac{1}{2\pi}\sum_n \iint_{\mathrm{BZ}} d^2k\, \Omega_n(\mathbf{k}), \tag{A2}$$

$$\Omega_n(\mathbf{k}) = -\sum_{n\neq n'} \frac{2\,\mathrm{Im}\langle\phi_{nk}|\frac{\partial H}{\partial k_x}|\phi_{n'k}\rangle\langle\phi_{n'k}|\frac{\partial H}{\partial k_y}|\phi_{nk}\rangle}{(E_n - E_{n'})^2}, \tag{A3}$$

where $\Omega_n(\mathbf{k})$ is the momentum-space Berry curvature for the nth band, and $\mathbf{k} = (\mathbf{k_x}, \mathbf{k_y})$ represents the Bloch wave vector in the first Brillouin zone. The summation of n runs over all occupied valence bands below the bulk gap. The absolute value of $\mathcal{C}$ corresponds to topological charges of the two-dimensional system. Niu and Thouless further show that the quantized Hall conductance is robust against disorders [58]. For a time-dependent Hamiltonian $H(t)$ without any specific periodicity, the many-body wave function satisfies

$$\Phi(x_1, \ldots, x_i + L, \ldots, x_N) = e^{i\kappa L}\Phi(x_1, \ldots, x_i, \ldots, x_N), \tag{A4}$$

where κ is introduced by the twisted boundary condition, and L is the size of the system. This is equivalent to solving a κ-dependent Hamiltonian:

$$H(\kappa, t) = \exp(i\kappa\sum x_i)H(t)\exp(-i\kappa\sum x_i), \tag{A5}$$

with the strict periodic boundary condition

$$\tilde{\Phi}(\kappa; x_1, \ldots, x_i + L, \ldots, x_N) = \tilde{\Phi}(\kappa; x_1, \ldots, x_i, \ldots, x_N). \tag{A6}$$

The Chern number and Berry curvature can be defined as follows:

$$\mathcal{C} = \frac{1}{2\pi}\int_0^T dt \int_0^{2\pi/L} dk\, \tilde{\Omega}_{kt}, \tag{A7}$$

$$\tilde{\Omega}_{kt} = -i\left[\left\langle \frac{\partial\tilde{\Phi}_0}{\partial\kappa}\middle|\frac{\partial\tilde{\Phi}_0}{\partial t}\right\rangle - \left\langle \frac{\partial\tilde{\Phi}_0}{\partial t}\middle|\frac{\partial\tilde{\Phi}_0}{\partial\kappa}\right\rangle\right], \tag{A8}$$

where $\tilde{\Phi}_0$ is the many-body ground state. The parameter space for κ $(0 < \kappa < 2\pi/L)$ and t $(0 < t < T)$ of Berry curvature is also a torus; even disorders exist. As long as the system remains an insulator during the whole process, the Hall conductance (Chern number) is still quantized [58,59]. Therefore, we can define Berry curvature in a nonperiodic space to evaluate the influence of disorders.

[1] P. W. Anderson, Phys. Rev. **109**, 1492 (1958).
[2] M. Onoda, Y. Avishai, and N. Nagaosa, Phys. Rev. Lett. **98**, 076802 (2007).
[3] A. Yamakage, K. Nomura, K. I. Imura, and Y. Kuramoto, J. Phys. Soc. Jpn. **80**, 053703 (2011).
[4] H. Obuse, A. Furusaki, S. Ryu, and C. Mudry, Phys. Rev. B **76**, 075301 (2007).
[5] K. S. Novoselov, A. K. Geim, S. V. Morozov, D. Jiang, Y. Zhang, S. V. Dubonos, I. V. Grigorieva, and A. A. Firsov, Science **306**, 666 (2004).
[6] K. S. Novoselov, A. K. Geim, S. V. Morozov, D. Jiang, M. I. Katsnelson, I. V. Grigorieva, S. V. Dubonos, and A. A. Firsov, Nature (London) **438**, 197 (2005).
[7] Y. Ren, Z. Qiao, and Q. Niu, Topological phases in two dimensional materials: A brief review, Rep. Prog. Phys. **79**, 066501 (2016).
[8] B. A. Bernevig, T. L. Hughes, and S.-C. Zhang, Science **314**, 1757 (2006).
[9] M. König, S. Wiedmann, C. Brüne, A. Roth, H. Buhmann, L. Molenkamp, X.-L. Qi, and S.-C. Zhang, Science **318**, 766 (2007).
[10] H. Aoki, Rep. Prog. Phys. **50**, 655 (1987).
[11] H. Aoki and T. Ando, Solid State Commun. **38**, 1079 (1981).
[12] R. Kubo, J. Phys. Soc. Jpn. **12**, 570 (1957).
[13] J. Guillemette, S. S. Sabri, B. Wu, K. Bennaceur, P. E. Gaskell, M. Savard, P. L. Lévesque, F. Mahvash, A. Guermoune, M. Siaj, R. Martel, T. Szkopek, and G. Gervais, Phys. Rev. Lett. **110**, 176801 (2013).
[14] J. H. García, L. Covaci, and T. G. Rappoport, Phys. Rev. Lett. **114**, 116602 (2015).
[15] J. H. Garcia and T. G. Rappoport, 2D Mater. **3**, 024007 (2016).
[16] F. Ortmann, N. Leconte, and S. Roche, Phys. Rev. B **91**, 165117 (2015).
[17] D. N. Sheng, L. Sheng, and Z. Y. Weng, Phys. Rev. B **73**, 233406 (2006).
[18] F. Evers and A. D. Mirlin, Rev. Mod. Phys. **80**, 1355 (2008).
[19] N. Leconte, F. Ortmann, A. Cresti, J.-C. Charlier, and S. Roche, 2D Mater. **1**, 021001 (2014).
[20] N. Leconte, F. Ortmann, A. Cresti, and S. Roche, Phys. Rev. B **93**, 115404 (2016).
[21] J. Sinova, S. O. Valenzuela, J. Wunderlich, C. H. Back, and T. Jungwirth, Rev. Mod. Phys. **87**, 1213 (2015).
[22] G. Vignale, J. Supercond. Nov. Magn. **23**, 3 (2010).
[23] J. Balakrishnan, G. K. W. Koon, A. Avsar, Y. Ho, J. H. Lee, M. Jaiswal, S.-J. Baeck, J.-H. Ahn, A. Ferreira, M. A. Cazalilla, A. H. Castro Neto, and B. Özyilmaz, Nat. Commun. **5**, 4748 (2014).
[24] J. Balakrishnan, G. K. W. Koon, M. Jaiswal, A. H. CastroNeto, and B. Özyilmaz, Nat. Phys. **9**, 284 (2013).
[25] N. F. Mott, Proc. R. Soc. London A **124**, 425 (1929).
[26] M. Gradhand, D. V. Fedorov, P. Zahn, and I. Mertig, Phys. Rev. Lett. **104**, 186403 (2010).
[27] E. McCann and M. Koshino, Rep. Prog. Phys. **76**, 056503 (2013).
[28] W.-K. Tse, Z. H. Qiao, Y. G. Yao, A. H. MacDonald, and Q. Niu, Phys. Rev. B **83**, 155447 (2011).
[29] Z. Qiao, S.A. Yang, W. Feng, W.K. Tse, J. Ding, Y. Yao, J. Wang, and Q. Niu, Phys. Rev. B **82**, 161414(R) (2010).
[30] Z. H. Qiao, W. Ren, H. Chen, L. Bellaiche, Z. Zhang, A. H. MacDonald, and Q. Niu, Phys. Rev. Lett. **112**, 116404 (2014).
[31] J. Wang, B. Lian, H. Zhang, Y. Xu, and S.-C. Zhang, Phys. Rev. Lett. **111**, 136801 (2013).
[32] H. Jiang, Z. H. Qiao, H.-W. Liu, and Q. Niu, Phys. Rev. B **85**, 045445 (2012).
[33] H. Pan, Z. Li, C.-C. Liu, G. Zhu, Z. H. Qiao, and Y. G. Yao, Phys. Rev. Lett. **112**, 106802 (2014).
[34] F. D. M. Haldane, Phys. Rev. Lett. **61**, 2015 (1988).
[35] C.-X. Liu, S.-C. Zhang, and X.-L. Qi, Annu. Rev. Condens. Matter Phys. **7**, 301 (2016).
[36] S. F. Qi, Z. H. Qiao, X. Z. Deng, E. D. Cubuk, H. Chen, W. G. Zhu, E. Kaxiras, S. B. Zhang, X. H. Xu, and Z. Y. Zhang, Phys. Rev. Lett. **117**, 056804 (2016).
[37] K. Nomura and N. Nagaosa, Phys. Rev. Lett. **106**, 166802 (2011).
[38] C.-Z. Chang, J. Zhang, X. Feng, J. Shen, Z. Zhang, M. Guo, K. Li, Y. Ou, P. Wei, L.-L. Wang, Z.-Q. Ji, Y. Feng, S. Ji, X. Chen, J. Jia, X. Dai, Z. Fang, S.-C. Zhang, K. He, Y. Wang, *et al.*, Science **340**, 167 (2013).
[39] K. Klitzing, G. Dorda, and M. Pepper, Phys. Rev. Lett. **45**, 494 (1980).
[40] R. B. Laughlin, Phys. Rev. B **23**, 5632 (1981).
[41] S. Kivelson, D.-H. Lee, and S.-C. Zhang, Phys. Rev. B **46**, 2223 (1992).
[42] D. N. Sheng and Z. Y. Weng, Phys. Rev. Lett. **78**, 318 (1997).
[43] R. Yu, W. Zhang, H. J. Zhang, S. C. Zhang, X. Dai, and Z. Fang, Science **329**, 61 (2010).
[44] C. X. Liu, X. L. Qi, X. Dai, Z. Fang, and S. C. Zhang, Phys. Rev. Lett. **101**, 146802 (2008).
[45] Z. H. Qiao, Y. L. Han, L. Zhang, K. Wang, X. Z. Deng, H. Jiang, S. Y. A. Yang, J. Wang, and Q. Niu, Phys. Rev. Lett. **117**, 056802 (2016).
[46] Z.-Q. Zhang, C.-Z. Chen, Y. Wu, H. Jiang, J. Liu, Q. feng Sun, and X. C. Xie, Phys. Rev. B **103**, 075434 (2021).
[47] C.-Z. Chen, H. Liu, H. Jiang, Q.-F. Sun, Z. Wang, and X. C. Xie, Phys. Rev. B **91**, 214202 (2015).
[48] R. Chen, D.-H. Xu, and B. Zhou, Phys. Rev. B **96**, 205304 (2017).
[49] Y. Kuno, Phys. Rev. B **100**, 054108 (2019).

[50] R. Chen, D.-H. Xu, and B. Zhou, Phys. Rev. B **100**, 115311 (2019).
[51] Z.-Q. Zhang, B.-L. Wu, J. Song, and H. Jiang, Phys. Rev. B **100**, 184202 (2019).
[52] Z. H. Qiao, X. Li, W.-K. Tse, H. Jiang, Y. G. Yao, and Q. Niu, Phys. Rev. B **87**, 125405 (2013).
[53] R.-L. Chu, J. Shi, and S.-Q. Shen, Phys. Rev. B **84**, 085312 (2011).
[54] *Electronic Transport in Mesoscopic Systems*, edited by S. Datta (Cambridge University Press, Cambridge, England, 1995).
[55] S. Y. A. Yang, Z. H. Qiao, Y. Yao, J. Shi, and Q. Niu, Europhys. Lett. **95**, 67001 (2011).
[56] X.-L. Qi, Y.-S. Wu, and S.-C. Zhang, Phys. Rev. B **74**, 085308 (2006).
[57] Q. Niu, D. J. Thouless, and Y. S. Wu, Phys. Rev. B **31**, 3372 (1985).
[58] Q. Niu and D. J. Thouless, J. Phys. A **17**, 2453 (1984).
[59] D. Xiao, M.-C. Chang, and Q. Niu, Rev. Mod. Phys. **82**, 1959 (2010).
[60] X. Z. Yu, Y. Onose, N. Kanazawa, J. H. Park, J. H. Han, Y. Matsui, N. Nagaosa, and Y. Tokura, Nature (London) **465**, 901 (2010).
[61] D. J. Thouless, M. Kohmoto, M. P. Nightingale, and M. den Nijs, Phys. Rev. Lett **49**, 405 (1982).
[62] M. C. Chang and Q. Niu, Phys. Rev. B **53**, 7010 (1996).